Supplementary Materials for

Structural basis for DNA damage-dependent poly(ADP-ribosyl)ation by human PARP-1

Marie-France Langelier, Jamie L. Planck, Swati Roy, John M. Pascal

correspondence to: John.Pascal@KimmelCancerCenter.org

This PDF file includes:

Table of Contents for Supplementary Materials

Materials and Methods

Gene cloning and mutagenesis

The following PARP-1 constructs were cloned into the NdeI/XhoI sites of the pET28 expression vector (Novagen): full-length wild-type (WT) PARP-1 (residues 1–1014) and mutants, Zn1 domain (residues 1–96), ΔCAT (residues 1-662), CAT domain WT (residues 662-1014) and mutant L713F and ΔZn2ΔBRCT (Δ97-206Δ381-484). The Zn3 domain (residues 216–366) and WGR-CAT fragment (residues 518-1014) were cloned into the NdeI/XhoI sites of the pET24 expression vector (Novagen). All mutations were performed using the QuikChange protocol (Stratagene) and verified by automated DNA sequencing.

Protein expression and purification

Full-length PARP-1 WT and mutants, the Zn1 and the Zn3 domains were expressed and purified as described previously using three chromatographic steps (*5, 10, 19, 25*): Ni^{2+} affinity, heparin-sepharose, and gel filtration. The ΔCAT fragment and ΔZn2ΔBRCT were purified as full-length. The WGR-CAT and CAT fragments were purified following the protocol used for full-length PARP-1 with the exception that the heparin column was equilibrated to 50 mM NaCl and the elution gradient was from 50 mM to 750 mM NaCl. Selenomethionine-containing Zn1, Zn3 and WGR-CAT were expressed in *Escherichia coli* grown in defined medium (*26*) and purified as WTs.

Crystallization of the PARP-1/DNA complex

In order to obtain crystals of PARP-1 in complex with DNA, it was necessary to exclude the non-essential Zn2 and BRCT domains. Attempts to crystallize full-length PARP-1 or combinations of PARP-1 domains that include Zn2 and/or BRCT have not been successful, probably due to the flexible modular architecture of full-length PARP-1. The domains of human PARP-1 were assembled on blunt-ended duplex DNA as a model for double-strand break damage. PARP-1 is potently activated by DNA double-strand breaks (*9, 10, 12, 19, 27*) and exhibits high binding affinity for blunt-ended DNA (*5, 9, 10, 17*).

Extensive crystallization screening using DNA length as a parameter identified the 26 base-pair length as being compatible with crystallization of the PARP-1 complex.

The PARP-1/DNA complex was formed by mixing native or selenomethionine-containing proteins (Zn1, Zn3, and WGR-CAT) at 300 μM with a 26-bp palindromic DNA duplex at 165 μM (5' GCCTACCGGTTCGCGAACCGGTAGGC 3') and adenosine diphosphate (ADP) at 500 μM in the following buffer: 25 mM Hepes pH 8.0, 150 mM NaCl, 1 mM EDTA, and 0.1 mM TCEP. Crystals were grown by sitting drop vapor diffusion at 20°C by mixing the PARP-1/DNA complex with an equal amount of 7% PEG 3350, 10% ethylene glycol, and 100 mM Hepes pH 7.5. Crystals were rapidly transferred to a solution of 3% PEG 3350, 25% ethylene glycol, 25 mM Hepes pH 7.5, 25 mM NaCl, 0.05 mM TCEP, and 500 μM ADP prior to flash-cooling in liquid nitrogen. X-ray diffraction data were collected at beamline X29A of the National Synchrotron Light Source (NSLS, Brookhaven National Laboratory), and processed using HKL2000 (*28*) or XDS (*29*) (Supplementary Table S1).

PARP-1/DNA complex structure determination

The PARP-1/DNA complex structure was determined by molecular replacement (MR) using the program PHASER (*30*) as implemented in the program package CCP4i (*31*). The x-ray structure of human CAT and the NMR structure of human WGR served as search models (PDB codes 3gjw and 2cr9, respectively). The x-ray structures of the Zn1 and Zn3 domains (PDB codes 3od8 and 2riq, respectively) were manually positioned into electron density observed in maps calculated with MR phases, and based on anomalous difference fourier maps calculated using MR phases and the anomalous signal from data collected at the zinc absorption edge (Table S1). The anomalous signal from data collected on selenomethionine-containing crystals at the selenium absorption edge (Table S1) confirmed the MR solution for the CAT and WGR domains, and confirmed the positioning of the Zn1 and Zn3 domains (Fig. S2B). The palindromic DNA duplex was modeled based on difference electron density that clearly indicated the position of the DNA within the complex. There are two PARP-1 complexes in the asymmetric unit of the crystal, with a PARP-1 complex bound to each terminus of the DNA duplex (Fig.

S2A). Each of the complexes appear to be nearly identical; however the PARP-1/DNA complex with chain labels A (Zn1), B (Zn3), and C (WGR-CAT) exhibited stronger electron density than the second complex in the asymmetric unit with chain labels D (Zn1), E (Zn3), and F (WGR-CAT). Structure illustrations have therefore been created using complex 1, with chain labels A, B, and C. PARP-1/DNA crystals exhibited diffraction anisotropy, and we found that applying anisotropic diffraction limits to the data assisted model building by improving the quality and level of detail in electron density maps. Anisotropic limits were imposed using the Diffraction Anisotropy Server at UCLA (*32*). The sphere of reflections was truncated using resolution cutoffs (3.3 Å, 3.7 Å, and 3.2 Å along the principal axes a, b, and c), and a B-factor correction was applied (-31.78 $Å^2$) as recommended by the Server. The final structure was refined against the entire sphere of reflections (Table S1). The C-terminal region of Zn3 in the PARP-1/DNA structure (residues 339 to 351) differed from that observed in the structure of the isolated Zn3, which formed a dimer in the crystal lattice that was mediated by this C-terminal region of Zn3. In the PARP-1/DNA structure the Zn3 domain is monomeric, with the C-terminus forming intradomain contacts. The electron density in this region was poorly defined; therefore only the mainchain was modeled in this region and the sidechains were truncated after the beta-carbon. The linker connecting the WGR and CAT domains was not visible in electron density maps and was therefore not modeled. Dissolved crystals that were analyzed on SDS-PAGE showed that the WGR-CAT polypeptide remained intact in the crystals and did not suffer from proteolysis (not shown); therefore we presume that the WGR-CAT linker region is not well-ordered in the PARP-1/DNA complex. A surface loop connecting the HD to the ART subdomain (residues 781 to 788) was poorly defined in electron density maps and therefore only the mainchain was modeled in this region and the sidechains were truncated after the beta-carbon. A WGR surface loop (residues 576 to 583) was not modeled due to apparent disorder. The model was constructed using COOT (*33*), and refined in REFMAC (*31*) using TLS and tight NCS and geometric restraints. The current refined model has an R/R_{Free} of 0.238/0.304 and exhibits good overall geometry (Table S1). 93.9 % of residues are located in the most favored region of the Ramachandran plot, and there are no residues located in disallowed regions.

Sedimentation Analysis

Sedimentation equilibrium and sedimentation velocity analyses were performed on a Beckman XL-I analytical ultracentrifuge using the 8-place An-50 Ti rotor, and a 6-sector centerpiece for equilibrium runs and a 2-sector centerpiece for velocity runs. Data were analyzed using the programs SEDFIT and SEDPHAT (*34, 35*). Sedimentation equilibrium analysis was performed using 1 μM PARP-1 in the absence or presence of 3 μM 8-mer DNA duplex. The 8-mer DNA duplex was fluorescently labeled for absorbance detection at 495 nm. Sedimentation velocity analysis was performed with 2.5 μM full-length PARP-1 in the absence or presence of 2.5 μM 8-mer DNA, and absorbance detection at 280 nm. The C(s) distribution analysis was performed using SEDFIT (*35*).

Gel shift assay

The gel shift assay was performed by incubating 1 μM of an 18-bp DNA duplex with 2 μM of each protein (Zn1, Zn3, WGR-CAT) alone or in combination for 30 min at 22°C in 50 mM Tris pH 7, 100 mM NaCl, 0.1 mM TCEP, 0.1 mM EDTA, 5% glycerol. Reactions were run on a 0.9% agarose gel for 35 min at 100V at 4°C in Tris-Borate (45 mM each) buffer. The gel was next stained in ethidium bromide.

SDS-PAGE PARP-1 automodification assay

The SDS-PAGE PARP-1 automodification assay was performed essentially as described (*5, 10, 19, 25*). PARP-1 full-length WT and mutants (1 μM) were preincubated with 1 μM of an 18-bp DNA duplex for 10 min at 22°C. 5 mM NAD^+ was then added to the reaction, and the mixture was incubated for various times before quenching with the addition of SDS loading buffer containing 0.1 M EDTA. The samples were resolved on SDS-PAGE and stained with Imperial Protein Stain (Pierce).

Colorimetric PARP-1 automodification assay

The colorimetric PARP-1 activity assay was performed essentially as described (*19, 25*). DNA-

dependent reactions using different combinations of PARP-1 fragments (Fig. 1B and FigS1) were performed as follow. 60 nM of each histidine-tagged protein (Zn1, Zn2, Zn3, WGR-CAT, full-length, ΔZn2ΔBRCT) were incubated with an 18-bp DNA duplex (200 nM) on a Ni^{2+}-chelating plate (5 PRIME) at 22°C in 40 μL. Reactions were started by the addition of 10 μL of a mixture of NAD^+ and biotinylated-NAD^+ (bio-NAD^+) at a 99:1 ratio, and a total concentration of 1000 μM were various time points. Reactions were quenched by the addition of 150 μL of 6 M guanidine hydrochloride (4.5 M final concentration). The reaction wells were washed three times with 200 μL of phosphate-buffered saline (PBS) containing 1% BSA (PBS/BSA). Streptavidin-conjugated horseradish peroxidase (Pierce) was added to each reaction for a 30-min incubation (1:12,000 dilution in PBS/BSA). Reaction wells were then washed three times with PBS/BSA. 75 μL of the streptavidin- conjugated horseradish peroxidase substrate Ultra-TMB (Pierce) was added to each reaction well, and this reaction was quenched with 75 μL of 2 N sulfuric acid. The absorbance at 450 nm (*A*450) was read on a Victor^{3}V (PerkinElmer Life Sciences); the absorbance at 550 nm (*A*550) was subtracted from the *A*450 reading to account for nonuniform variations in the plastic plates. A biotinylated, histidine-tagged peptide (biotin-Ser-Trp-His-His-His-His-His-His-His-His) of known concentration was immobilized on the Ni^{2+} plate and served as a standard for converting the *A*450 reading into a quantity of biotin. The amount of ADP-ribose was then estimated as 100 times the amount of biotin, following the 99:1 ratio of NAD^+ to $bNAD^+$. A background *A*450 reading was performed for each NAD^+ concentration in the absence of PARP-1 to account for nonspecific binding of $bNAD^+$ and streptavidin-conjugated horseradish peroxidase to the reaction well. DNA-independent reactions using full-length PARP-1 WT or CAT and mutants (Fig. 4E, Fig.S7, S9, S10) were performed using 60 nM of protein and various concentrations of NAD^+:bio-NAD^+ (99:1 ratio). Michealis-Menten constants were determined by measuring initial rate of reactions at various NAD^+ concentrations. Fitting the Michealis-Menten model to the data yielded a K_m, V_{max} and k_{cat}. The values presented in Fig. S9 represent the average of 3 independent experiments.

Radioactive PARP-1 automodification assay

The DNA-independent activity of WT PARP-1 and mutants was tested by incubating 500 nM protein with a mixture of radiolabeled ^{32}P NAD^+ (0.16 μCi; 0.2 μM) and unlabeled NAD^+ (99.8 μM) for 10 minutes at RT in reaction buffer (20 mM Tris pH 7.5, 50 mM NaCl, 5 mM $MgCl_2$, 0.1 mM TCEP). The 10 μL reactions were stopped by the addition of 2 μl of loading buffer, resolved on 12% SDS-PAGE, and exposed on phosphorimager.

Differential scanning fluorimetry

Differential scanning fluorimetry experiments were performed using 5 μM protein and 5X Sypro Orange (Invitrogen) in a final volume of 20 μL. Fluorescence emission was measured while the temperature was increased from 25 to 95°C (1°C intervals) in an Applied Biosystems Step One RT-PCR. The relative melting temperature (T_M) for each protein was calculated by fitting a Boltzmann sigmoid to the temperature-dependent change in fluorescence emission. In Fig. 4F, the T_M value of WT PARP-1 was subtracted from the T_M of PARP-1 mutants to obtain ΔT_M. In Fig. 4G, the T_M value obtained in the absence of DNA was subtracted from the T_M value obtained in the presence of DNA to yield ΔT_M. ΔT_M values in Fig. 4F, G represent the average of 3 to 5 independent experiments.

SOM Text

Model of full-length PARP-1

The PARP-1/DNA complex provides the relative locations of the N- and C-terminus for each of the essential domains, and thus allowed us to model the positions of the Zn2 and BRCT domains using available structures (PDB code 3odc for Zn2 and 2cok for BRCT). The Zn2 domain was positioned between the C-terminus of the Zn1 domain and the N-terminus of the Zn3 domain, which both extend in the same direction in the PARP-1/DNA complex and are located ~28 Å apart. The termini of the Zn2 domain are located over 20 Å apart, and there are ~15 linker residues between Zn1 and Zn2, and ~20 linker residues between Zn2 and Zn3. Thus, the PARP-1/DNA complex can easily accommodate the modeled position of the Zn2 domain. The BRCT domain was positioned between the C-terminus of Zn3 and the N-terminus of WGR, which are ~60 Å apart in the PARP-1/DNA complex. The region between the Zn3 and WGR domain has multiple PAR acceptor sites and has thus been termed the automodification domain (AD). The AD contains a BRCT fold and collectively has 76 linker residues: the Zn3 to BRCT linker has 28 residues, and the BRCT to WGR linker has 48 residues. The termini of the BRCT fold are located ~25 Å apart. Thus, the BRCT domain and the linker residues are capable of spanning the distance between the Zn3 C-terminus and the WGR N-terminus as seen in the PARP-1/DNA complex. The assembled model for full-length PARP-1 is a first approximation of the location of the Zn2 and BRCT domains within the PARP-1/DNA complex.

There are several instructive aspects of the model of full-length PARP-1 in complex with DNA. The Zn2 domain extends away from the main body of the PARP-1 assembly, and can therefore explain why deletion of the Zn2 domain has no affect on activation of PARP-1 by DNA double-strand breaks. The linker residues that remain after deletion of Zn2 presumably still allow the Zn1 and Zn3 domains to adopt their side-by-side conformation. Another compelling feature is that the BRCT fold and associated linker residues (collectively the AD) are anchored between the Zn3 and WGR domain, in close proximity to the CAT and available for *in cis* modification. The juxtaposition of the AD and the CAT can explain

the preference of PARP-1 to perform automodification of itself over heteromodification of other target proteins. The anchoring of the AD next to the CAT could also contribute to the ability of PARP-1 to synthesize long chains of PAR, by persistently holding substrate near the active site. The model also explains how the BRCT domain can function to recruit its binding partners to the PARP-1 catalytic domain for heteromodification. Lastly, the positioning of the AD next to the CAT could contribute to the increase in catalytic rate of poly(ADP-ribosyl)ation through enhanced proximity of the protein substrate.

Monomeric interaction of PARP-1 with DNA

Previous studies have suggested that PARP-1 dimerization on DNA is necessary for activation (*36, 37*). However, recent structural studies have reported a monomeric interaction of PARP-1 with DNA, including an NMR study of a Zn1-Zn2 fragment on DNA (*6*), crystal structures of the individual Zn1 and Zn2 domains on DNA (*5*), a SAXS analysis of a PARP-1 fragment (Zn1-Zn2-Zn3-BRCT) on DNA (*17*), an electron microscopy study of full-length PARP-1 on DNA in complex with DNA-PK (*18*), and the study presented here. Collectively, the structural studies indicate that PARP-1 interacts with DNA as a monomer, and suggest that dimerization on DNA is not essential for PARP-1 activation. Biochemical results that have shown complementation between inactive PARP-1 mutants (*12, 19*) or fragments of PARP-1 (*11, 19*) are likely to reflect the modular nature of PARP-1 domains and their abilities to operate *in trans* (Fig. S1), rather than a strict requirement for dimerization.

HD distortions and CAT domain access to substrates

It is not expected that HD distortion will influence CAT domain access to substrate NAD^+ since DNA-dependent activity does not change the affinity for NAD^+ (*19*), and the structures of isolated CAT domains have an active site that is accessible to inhibitors. Moreover, CAT domain active site structures determined in the absence of DNA and regulatory domains are accessible for protein substrates, as indicated by molecular dynamics calculations that have docked into a rigid catalytic active site the extended peptides derived from histone tails that are modified by PARP-1 (*38*). Accessibility to extended

peptides is particularly relevant because all of the PARP-1 automodification sites identified to date exist in the AD linker regions, outside of structured domains (*12, 39*). Thus, the observed HD distortions are unlikely to have a significant influence on access to NAD^+ substrate or target protein substrate. Rather, we propose that distortions to the structure and stability of HD are linked to the stability of ART, and that changes in the stability and conformational dynamics of the ART subdomain underlie the DNA-dependent activation mechanism (Fig. S11).

a

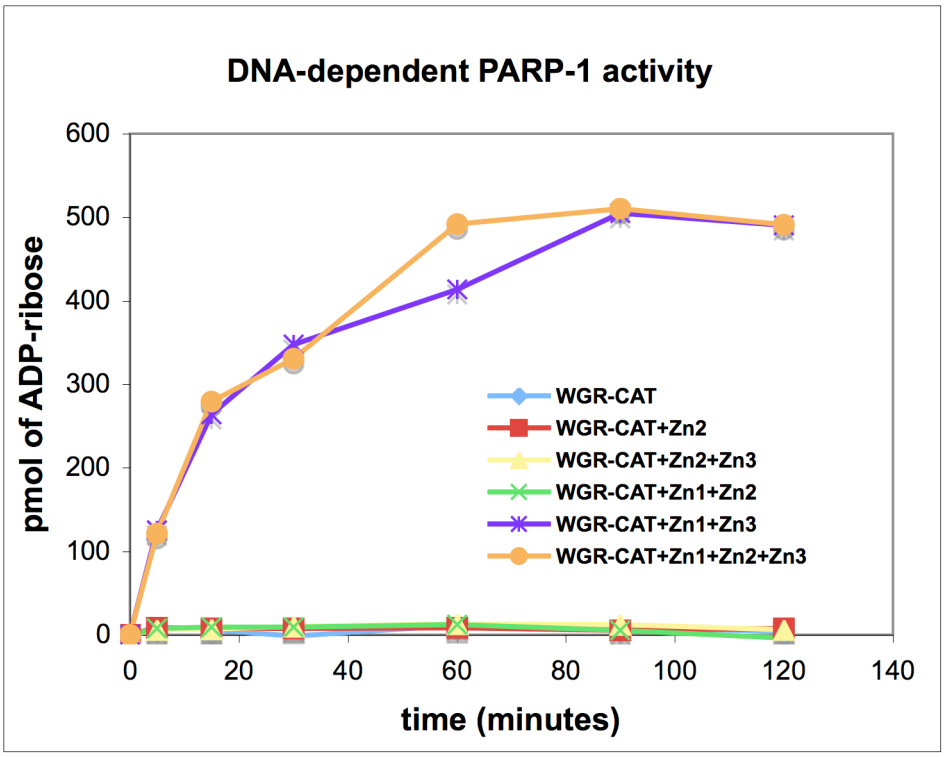
DNA-dependent PARP-1 activity
pmol of ADP-ribose
600
500
400
300
200
100
0
0
20
40
60
80
100
120
140
time (minutes)
WGR-CAT
WGR-CAT+Zn2
WGR-CAT+Zn2+Zn3
WGR-CAT+Zn1+Zn2
WGR-CAT+Zn1+Zn3
WGR-CAT+Zn1+Zn2+Zn3

b

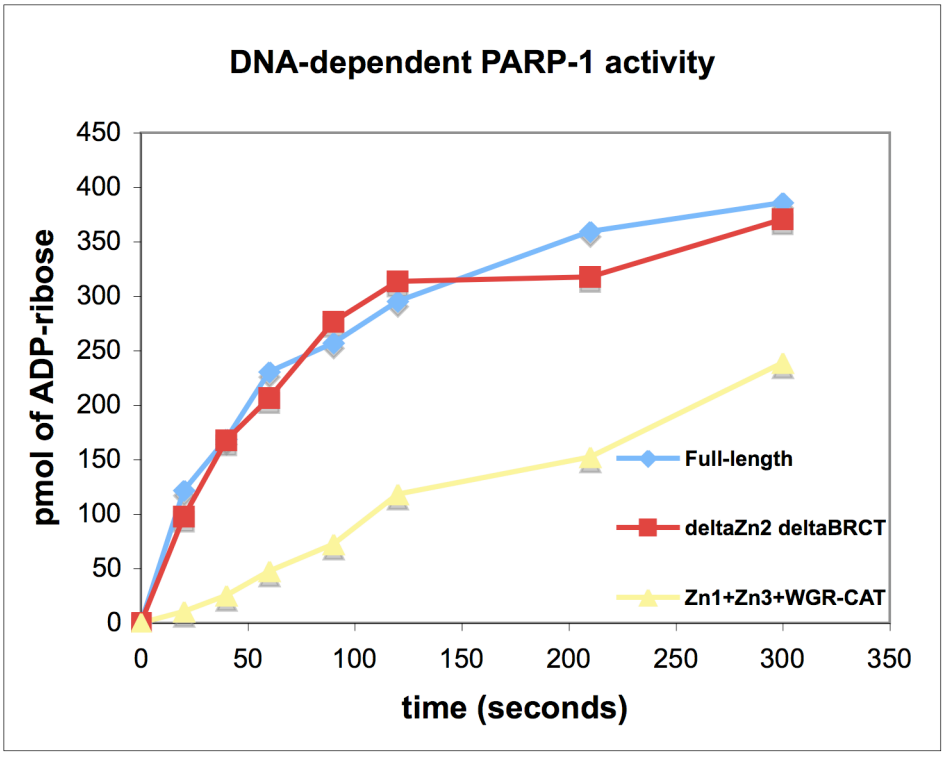
DNA-dependent PARP-1 activity
pmol of ADP-ribose
450
400
350
300
250
200
150
100
50
0
0
50
100
150
200
250
300
350
time (seconds)
Full-length
deltaZn2 deltaBRCT
Zn1+Zn3+WGR-CAT

Fig S1. Colorimetric assay of PARP-1 DNA-dependent automodification measuring ADP-ribose formation over time. a DNA-dependent reactions were performed with 60 nM of each protein (Zn1, Zn2, Zn3, WGR-CAT) and 200 nM of an 18-bp DNA duplex for various time points. **b**. DNA-dependent reactions were performed as in **a** with Zn1, Zn3, WGR-CAT, full-length, and ΔZn2ΔBRCT for shorter time points. The results indicate that Zn2 is not required for PARP-1 activation by double-strand break DNA and Zn2 cannot replace Zn1 in its function in PARP-1 activation on double-strand break, consistent with previous studies (*5, 12*). Zn2 has been suggested to be important for PARP-1 DNA-dependent activity on other types of DNA damage (*6, 40, 41*). The results further indicate that the BRCT is dispensable for PARP-1 DNA-dependent activity as previously shown (*12, 15*). PARP-1 modifies itself primarily on sites in the AD, but automodification has been shown to happen outside of this region (*12, 39*), explaining why automodification can be monitored in the absence of the AD in this experiment. Panel **b** indicates that even though a PARP-1 polypeptide lacking both the Zn2 and BRCT domains shows a level of DNA-dependent activity similar to full-length PARP-1, the use of a combination of the isolated Zn1, Zn3 and WGR-CAT fragments results in a 5-fold reduction in PARP-1 DNA-dependent activity as measured at the 60 second time point. This is most likely due to the fact that the domains are physically separated in the combination experiment.

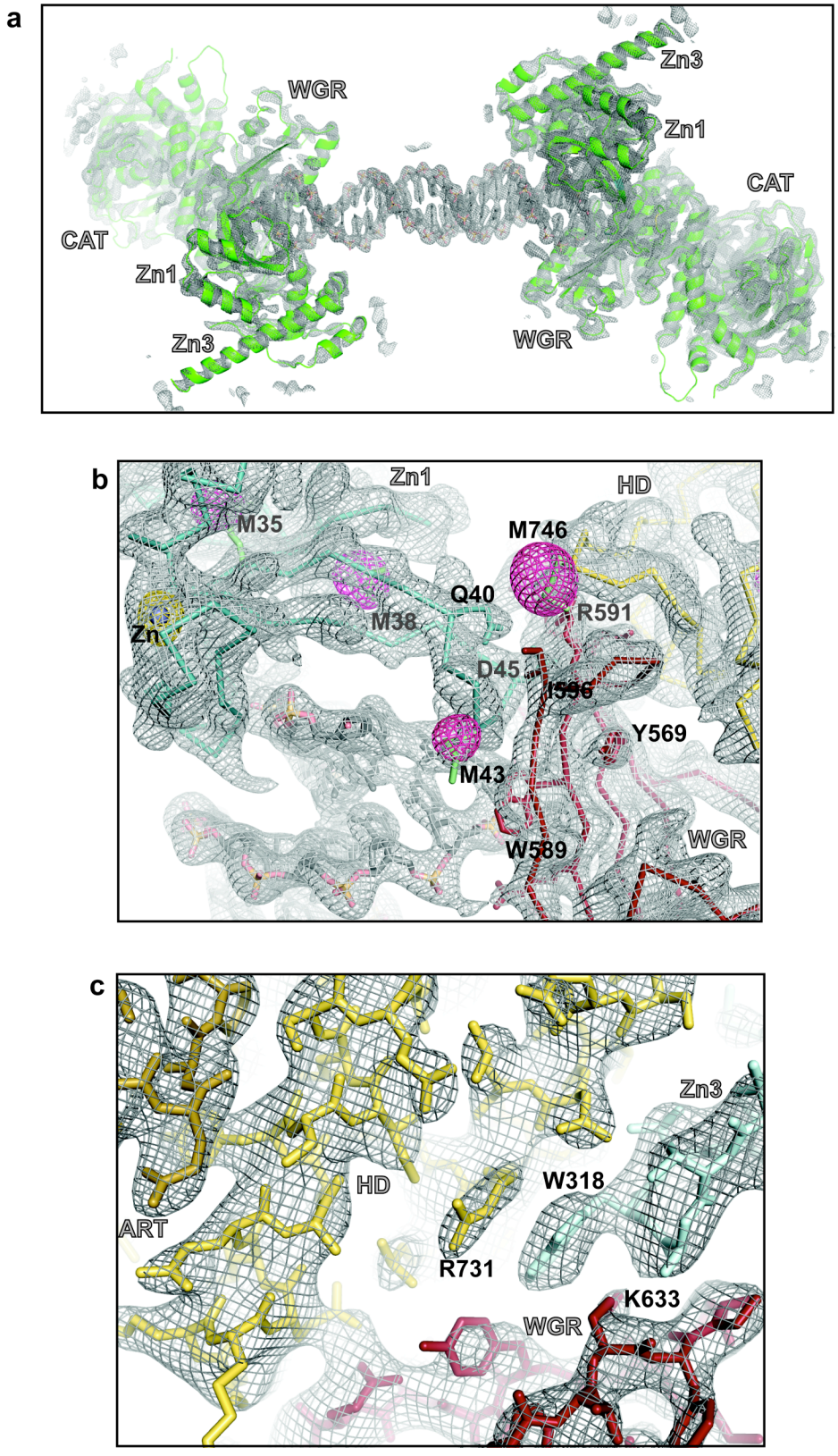
a
WGR
Zn3
Zn1
CAT
CAT
Zn1
Zn3
WGR
b
Zn1
HD
M35
M746
Q40
R591
Zn
M38
D45
I556
Y569
M43
W589
WGR
c
Zn3
HD
W318
ART
R731
K633
WGR

Fig. S2. Electron density maps for the refined PARP-1/DNA structure.

a. A 3.3 Å σA-weighted $2F_O–F_C$ electron density map created using coefficients calculated in REFMAC (*31*) and contoured at 1.4σ. The entire content of the asymmetric unit is shown, with a PARP-1 complex bound to each end of the 26-bp DNA. Each of the PARP-1 domains are depicted in cartoon representation and labeled.
b. A 3.3 Å σA-weighted $2F_O–F_C$ electron density map created using coefficients calculated in REFMAC and contoured at 1.2σ (drawn in grey). Anomalous difference Fourier maps are shown for data collected at the zinc edge (yellow, 8.0 σ) and for data collected at the selenium edge (pink, 6.0 σ). The zinc atom of the Zn1 domain is labeled and shown as a grey sphere. Methionine side chains are drawn as sticks and labeled. For reference, some of the residues involved in the Zn1–WGR–HD interface or the WGR interface with DNA are drawn as sticks and labeled.
c. A 3.3 Å σA-weighted $2F_O–F_C$ electron density map created using coefficients calculated in REFMAC and contoured at 1.2σ is drawn in grey. The coordinates of the refined PARP-1/DNA model are overlaid and drawn as sticks. The domains are labeled and colored (Zn3, cyan; WGR, red; HD, yellow). For reference, some of the residues involved in the Zn3–WGR–HD interface are labeled.

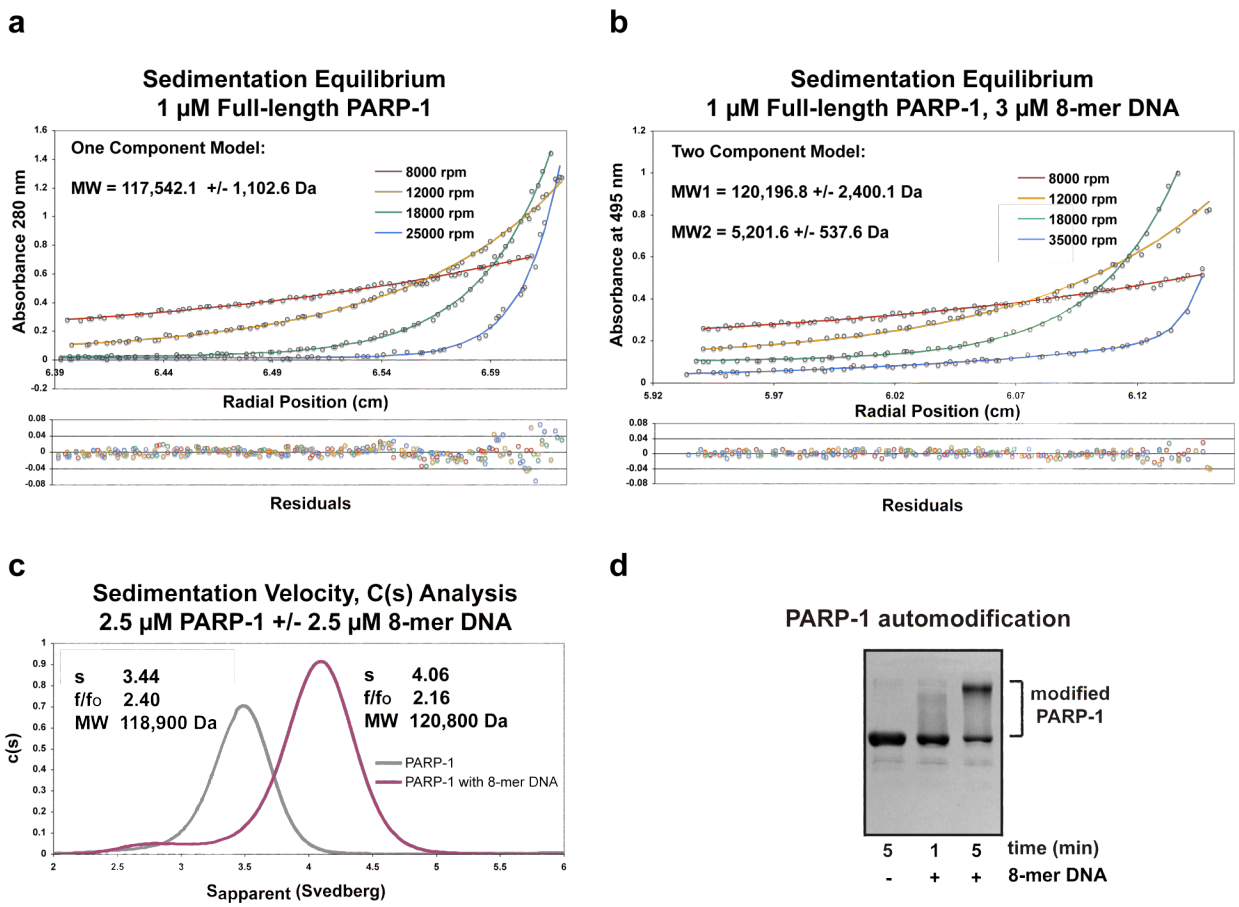

Fig. S3. Sedimentation analysis of full-length human PARP-1 bound to DNA

a. Sedimentation equilibrium analysis of full-length PARP-1. PARP-1 at 1 µM loading concentration was sedimented to equilibrium at 8000, 12000, 18000, and 25000 rpm in a Beckman XL-I Analytical Ultracentrifuge using a An 50 Ti rotor. Radial absorbance scans measured at 280 nm determined the distribution of PARP-1 in the centrifugal field. Data analysis was performed using SEDFIT and SEDPHAT. A single component model yielded the best fit to the data. The calculated molecular weight (MW) of 117,542 Da is in good agreement with the MW expected for full-length PARP-1 (115,299 Da), indicating that PARP-1 is a monomer in solution.

b. Sedimentation equilibrium analysis of full-length PARP-1 bound to DNA. PARP-1 (1 µM) was incubated with a fluorescently labeled 8-mer DNA duplex (3 µM), and the mixture was sedimented to equilibrium at 8000, 12000, 18000, and 35000 rpm. Radial absorbance scans measured at 495 nm determined the distribution of fluorescently labeled 8-mer DNA in the centrifugal field. PARP-1 does not absorb at 495 nm; therefore only the DNA contributes to the absorbance signal. A two component model yielded the best fit to the data. One component is the population of free DNA that sediment at a calculated MW of 5,202 Da (predicted MW 5,359 Da). A population of free DNA is consistent with the excess of DNA in the loaded mixture. The second component is the population of DNA bound to PARP-1 that sediment at a calculated MW of 120,197 Da. The calculated MW indicates that PARP-1 binds as a monomer to DNA with a 1:1 stoichiometry (predicted MW of the complex 120,657 Da).

c. Sedimentation velocity analysis of full-length PARP-1 in the absence and presence of DNA. A sedimentation velocity experiment was performed with full-length PARP-1 (2.5 µM), or a mixture of full-length PARP-1 (2.5 µM) and 8-mer DNA (2.5 µM). Data analysis was performed using SEDFIT. The presented C(s) analysis represents the distribution of sedimenting species. For both of the conditions

shown, a single peak represents ~95% of the distribution, indicating a homogenous solution. The apparent sedimentation coefficient (s, in Svedbergs) and the frictional ratio (f/f_O) were fit to the data. The MW shown were calculated based on the fitted sedimentation coefficients and frictional ratios, and are in excellent agreement with the results of the sedimentation equilibrium experiments in **a** and **b**, further indicating that PARP-1 exists as a monomer and binds to DNA as a monomer. The sedimentation velocity analysis further indicates that PARP-1 exists as a highly extended molecule in the absence of DNA, and that binding to DNA creates a more compact conformation of PARP-1 that sediments faster and with lower frictional ratio, consistent with the presented model for full-length PARP-1.
d. An SDS-PAGE PARP-1 automodification assay demonstrates that an 8-mer DNA duplex activates PARP-1. PARP-1 (1 μM) was incubated with or without DNA (1 μM) as shown for the indicated time points.

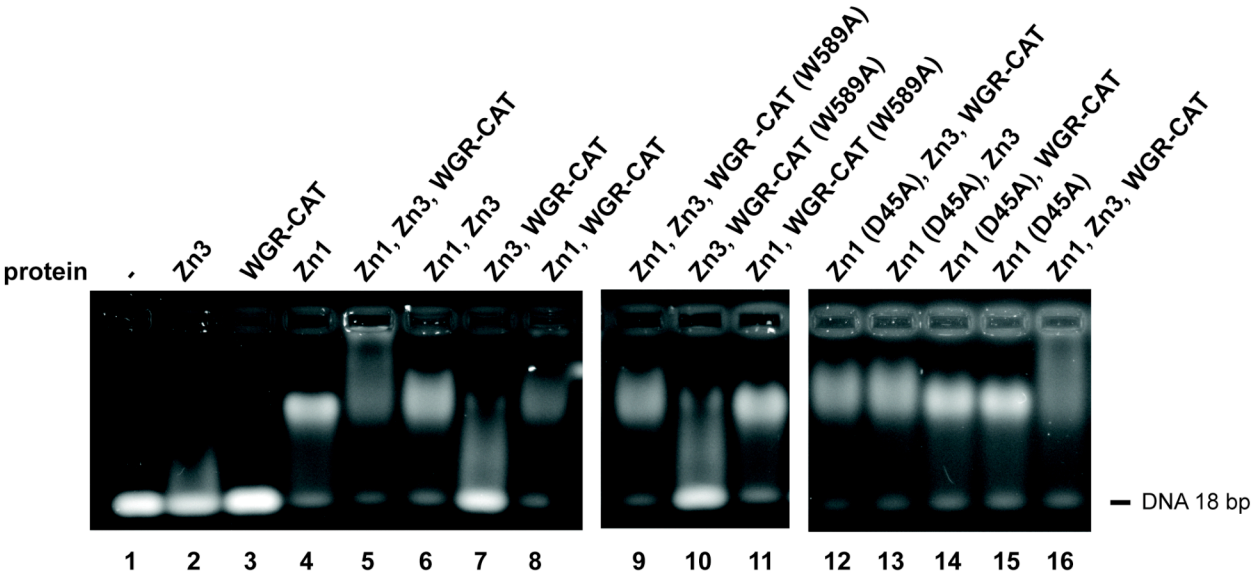

Fig. S4. The Zn1, Zn3, and WGR-CAT collaboratively bind to DNA.
DNA binding gel shift assay. Wild-type or mutant Zn1, Zn3, and WGR-CAT domains (2 μM each) were assembled on an 18 bp DNA duplex (1 μM) in the combinations listed above the gel. Reactions were resolved by electrophoresis on a 0.9% agarose gel, and subsequently stained with ethidium bromide. Lane 1 shows the migration of DNA probe in the absence of protein. The Zn1 domain shifts the DNA probe on its own (lane 4), whereas the Zn3 exhibits only a minor shift in mobility (lane 2) and the WGR-CAT shows no apparent shifting of the probe on its own (lane 3). In combination, the Zn1, Zn3 and WGR-CAT collaborate to form a complex on DNA, represented by a supershift of the Zn1-DNA complex (lanes 5 and lane 16). Lanes 6-8 show that pairs of combinations of domains yield minor shifts, but do not produce the supershift seen when all three components are added, thus indicating that Zn1, Zn3 and WGR-CAT bind together to DNA. As a control, WGR-CAT mutant W589A was unable to interact with the Zn1-Zn3-DNA complex (lane 9) or the Zn1-DNA complex (lane 11). W589 contacts DNA in the PARP-1/DNA structure (Fig. 2). As a second control, the Zn1 mutant D45A can bind to DNA (lane 15) and interact with Zn3 (lane 13), but it cannot interact with the WGR-CAT fragment on DNA (lane 14), and it cannot form the supershift (lane 12). D45 is involved in an interdomain contact with WGR in the PARP-1/DNA structure (Fig. 3C).

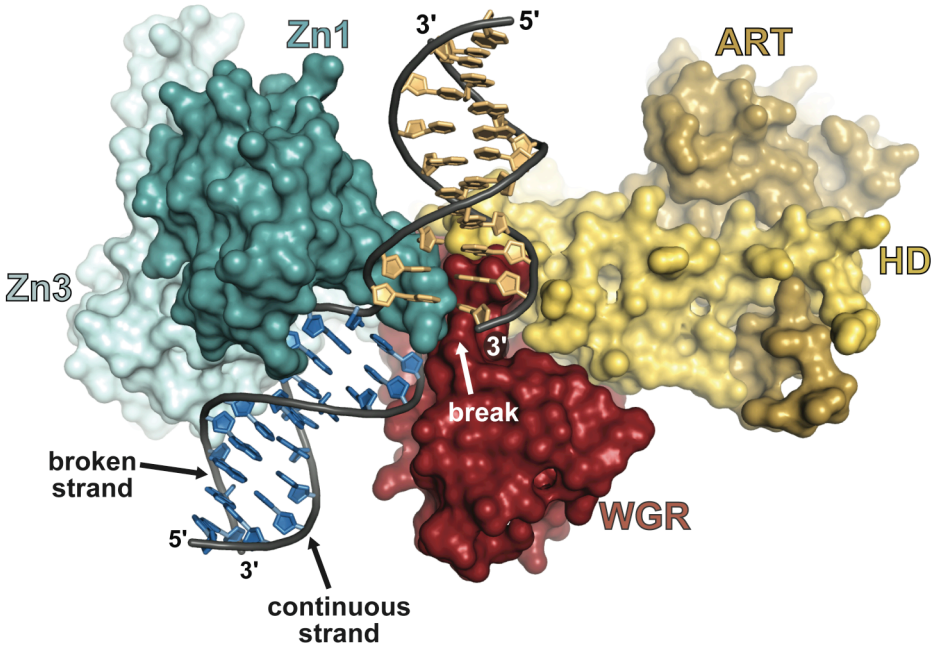

Fig. S5. Model for PARP-1 binding to a nicked DNA substrate.
The assembly of PARP-1 domains was modeled in complex with a DNA duplex containing a single strand break, or nick in the phosphate backbone. A 20-base pair (bp) duplex with a centrally placed nick was aligned to the DNA duplex present in the PARP-1/DNA structure, such that the site of the single strand break coincided with the site of the double strand break in the PARP-1/DNA structure (duplex with blue base pairs). The second half of the nicked DNA duplex was positioned so that there were no clashes with PARP-1 (duplex with orange base pairs). The location of WGR at the 5′ end of the DNA in the PARP-1/DNA structure prevents the continuous, unbroken DNA strand from being modeled next to the WGR due to steric clashes with the PARP-1/DNA complex. Modeling of the nicked DNA requires a bend at the nick, which is consistent with an electron microscopy study that observed an increase in the bending angle of nicked DNA upon interaction with PARP-1 (*42*). The PARP-1/DNA structure and the model of PARP-1 bound to a nick illustrate that PARP-1 has a defined polarity at DNA ends, with the Zn1 domain oriented on the 3′ end and the WGR occupying the 5′ end. Due to the polarity of the PARP-1/DNA interaction with DNA ends, it is not possible for two PARP-1 molecules to bind to a nick or a gap in the DNA duplex.

a

PARP-1 structure PDB code	r.m.s.d. (Å), HD / ART		
	PARP-1/DNA HD / ART	1a26 HD / ART	1wok HD / ART
3gjw	1.55 / 0.89	0.92 / 0.93	0.90 / 0.92
1wok	1.66 / 0.80	0.82 / 0.73	–
1a26	1.64 / 0.75	–	–

b

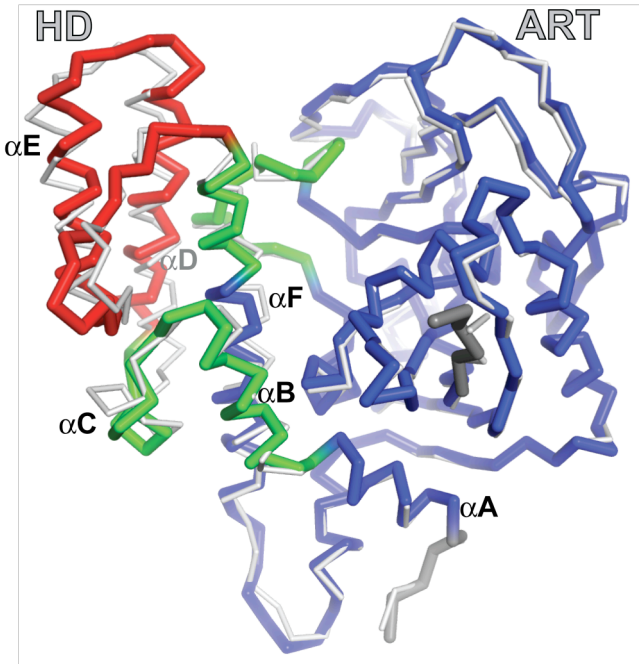

Fig. S6. CAT domain movements and distortion of the HD
The HD structure is distorted in the PARP-1/DNA complex compared to other HD structures determined in the absence of regulatory domains and DNA (PDB codes 3gjw, 1wok, and 1a26). In contrast, the ART structure in the PARP-1/DNA complex is similar to other ART structures determined in the absence of regulatory domains and DNA.
a. R.m.s.d. values for alignment of HD or ART subdomains of PARP-1 structures. The alignments include the alpha carbon atoms of residues 664–779 of the HD, and residues 788–1009 of the ART. The PDB codes are as follows: 3gjw, human PARP-1 determined at 2.3 Å; 1wok, human PARP-1 determined at 3.0 Å; 1a26, chicken PARP-1 determined at 2.3 Å.
b. PARP-1 CAT domain colored to indicate "mobile" regions identified through comparison of the CAT in the PARP-1/DNA complex to CAT structures determined in the absence of regulatory domains. Analysis was performed using DYNDOM (*43*). Color code: blue, fixed domain; red, moving domain; green, hinge region. The structure of the CAT domain determined in the absence of regulatory domains is shown in light grey (1a26), and is representative of all three structures analyzed.

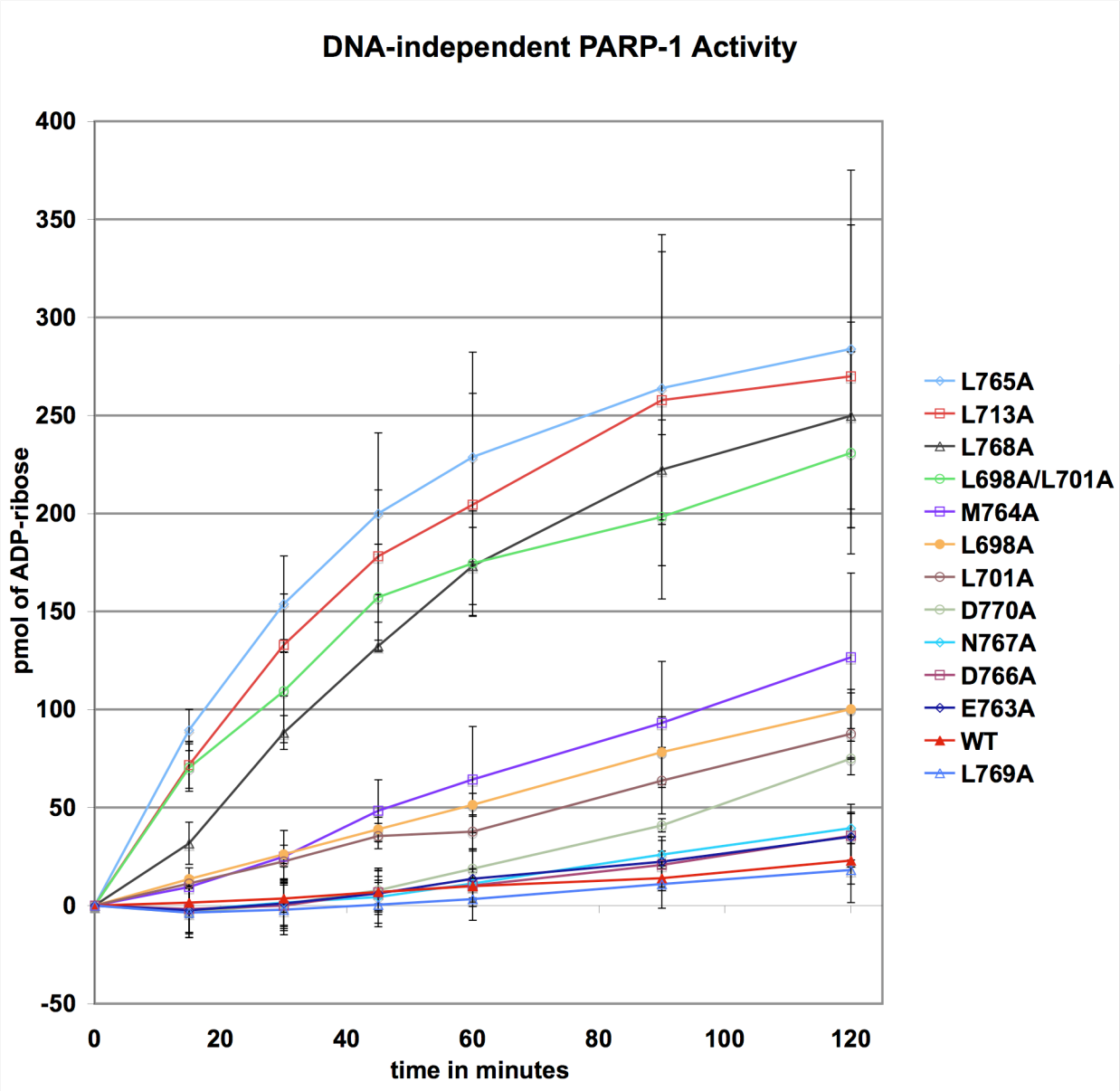

Fig. S7. DNA-independent PARP-1 automodification using the colorimetric assay. Full-length WT PARP-1 and HD mutant activities were measured at the indicated time-points. The values represent the average of three independent experiments, and the error bars represent the standard deviations. The 90-minute time-point is presented in Fig. 4E.

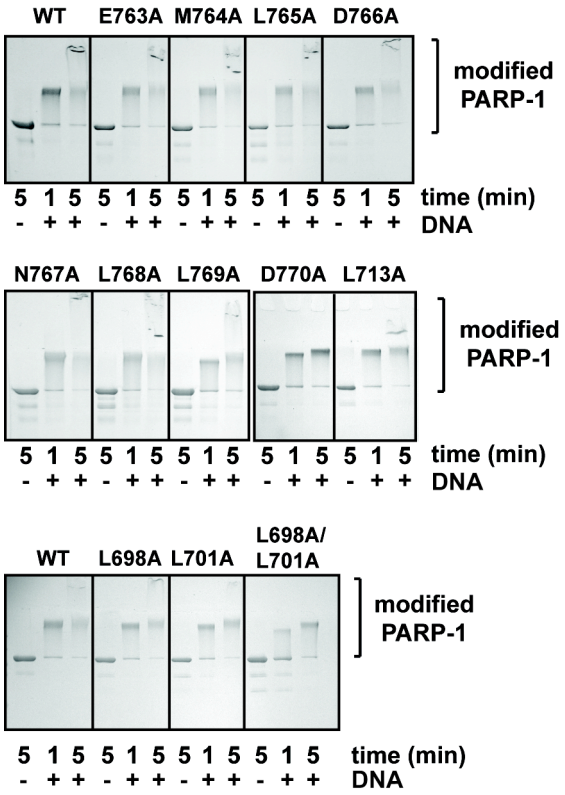

Fig. S8. SDS-PAGE assay of DNA-dependent PARP-1 automodification. The full-length PARP-1 HD mutants were tested for their DNA-dependent activity. Full-length WT PARP-1 and mutants were monitored for a shift in migration due to the covalent addition of PAR at the indicated time points. The presence or absence of DNA is noted. The HD hydrophobic core mutants did not show an increased level of DNA-dependent activity compared to WT PARP-1, indicating that these mutations act through the same mechanism as DNA to stimulate PARP-1 catalytic activity. DNA-independent activity is not observed in this case (see minus DNA lanes for WT and mutants) compared to the colorimetric and radioactive assays due to the lower sensitivity of the SDS-PAGE assay.

a

DNA-independent PARP-1 automodification activity

	Km (µM)	*Vmax* (µmol/min*mg)	*Kcat (1/s)*
WT	188.0 +/- 43.8	0.0017 +/- 0.0002	0.0032 +/- 0.0004
L765A	305.9 +/- 77.4	0.036 +/- 0.004	0.069 +/- 0.008
L768A	138.1 +/- 53.2	0.017 +/- 0.004	0.033 +/- 0.008
L713A	264.5 +/- 54.1	0.031 +/- 0.006	0.059 +/- 0.01

b

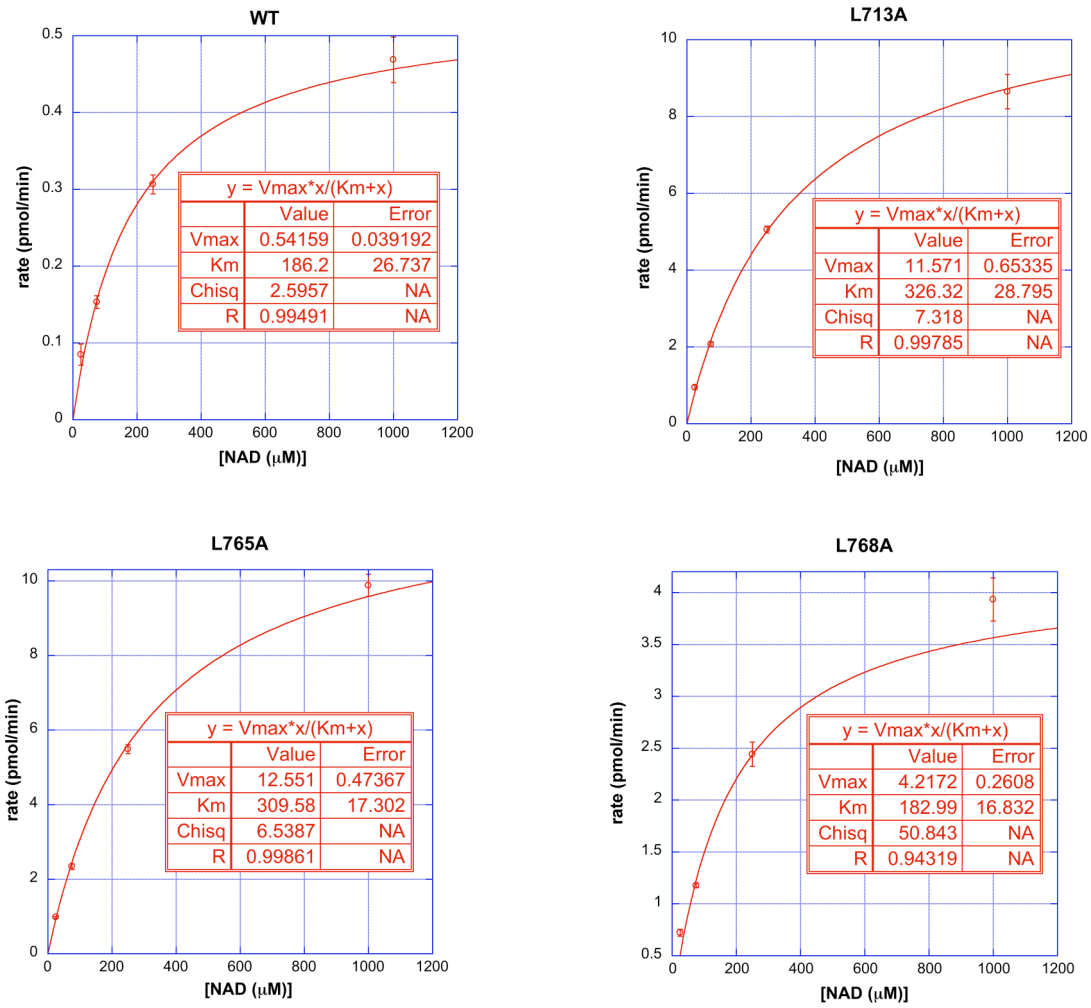

Fig. S9. Kinetics of PARP-1 WT and HD mutants automodification performed using a colorimetric assay. Time points in the linear portion of the reaction profile were measured for several NAD^+ concentrations to provide initial rates in pmol of ADP-ribose/min. Initial rates were plotted versus total NAD^+ concentration and fitted using the Michaelis-Menton model to the data and yielded K_M (µM) and V_{MAX} (pmol/min). **a**. Kinetic parameters obtained by fitting the Michaelis-Menten model to the data. The values represent the average of three independent experiments and their standard deviation. **b**. Example of a Michaelis-Menton plot of a DNA-independent experiment for WT, L765A, L768A and L713A mutant. The reactions were performed with 60 nM protein. DNA is a V-type allosteric regulator of PARP-1 activity, increasing the rate of the reaction (V_{MAX}) but having no effect on the affinity for substrate NAD^+ (K_M) (*19*). The HD mutants with elevated DNA-independent

activity are expected to simulate the effect of DNA on PARP-1 activity. The Michealis-Menten constants V_{MAX} and K_M determined for the HD mutants L765A, L768A, and L713A each showed an increase in V_{MAX} compared to WT PARP-1, but the K_M for NAD^+ remained unchanged. Thus, PARP-1 binding to DNA breaks and mutations in the hydrophobic core of the HD act through a similar mechanism to stimulate PARP-1 catalytic activity.

a

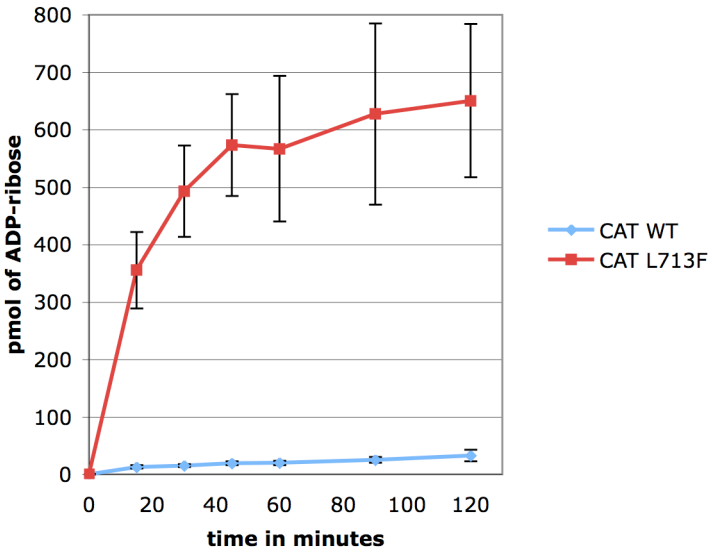
800
700
600
500
400
300
200
100
0
pmol of ADP-ribose
0
20
40
60
80
100
120
time in minutes
CAT WT
CAT L713F

b

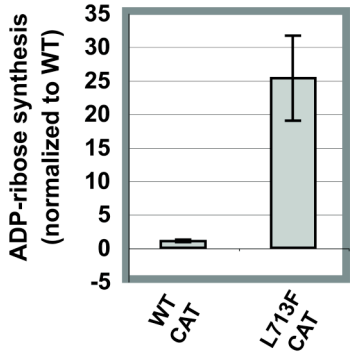
35
30
25
20
15
10
5
0
-5
ADP-ribose synthesis
(normalized to WT)
WT
CAT
L713F
CAT

c

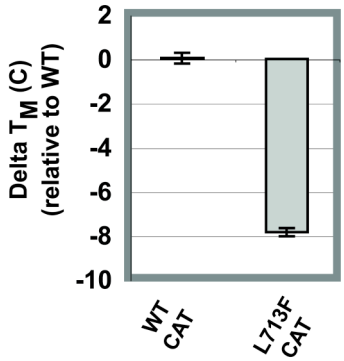
2
0
-2
-4
-6
-8
-10
Delta T M (C)
(relative to WT)
WT
CAT
L713F
CAT

d

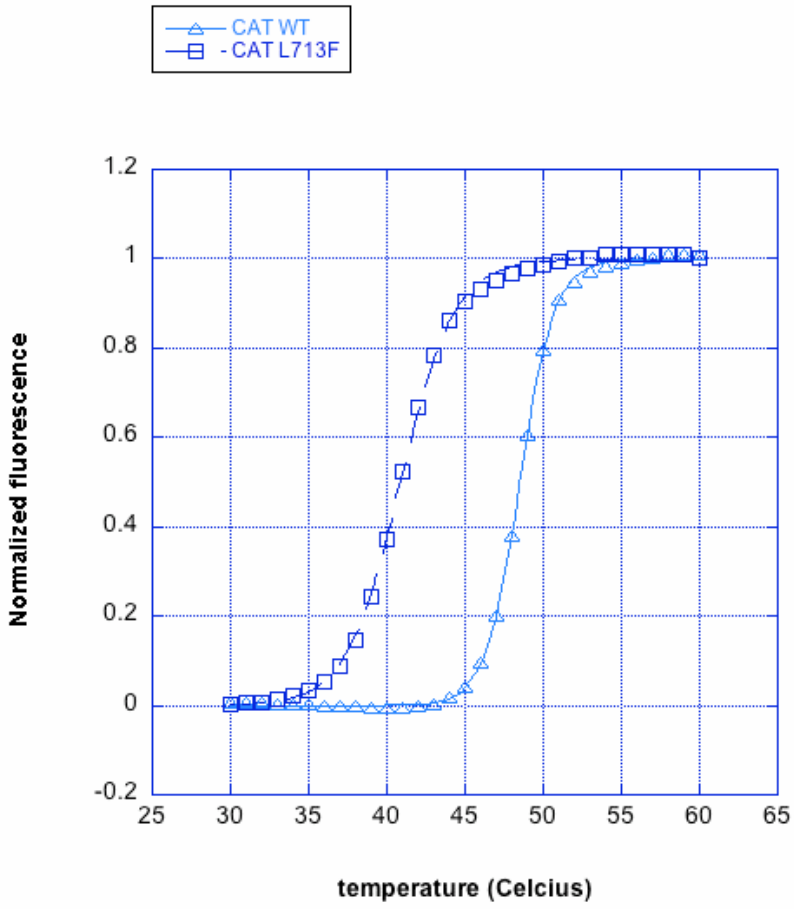

Fig. S10. DNA-independent activity and thermal stability of the isolated CAT domain. a. CAT WT (residues 661-1014) and CAT L713F mutant DNA-independent activities were measured at the indicated time-points using the colorimetric assay. The values represent the average of three independent experiments, and the error bars represent the standard deviations. **b**. The 90-minute time-point from the experiment shown in **a**. is presented as a fold increase over WT. **c**. ΔT_M were calculated by subtracting the T_M of WT CAT (residue 661-1014) from the T_M of the CAT mutant L713F. The T_M were obtained by differential scanning fluorimetry. The values presented are an average of 3 to 5 independent experiments. **d.** An example of Melting curves obtained by differential scanning fluorimetry for the CAT WT and CAT mutant L713F. The normalized fluorescence was obtained using the following formula: $(F_0-A_0)/(A_{max}-A_0)$, where F_0 is the fluorescence measured at one specific temperature and A_{max} and A_0 are obtained by fitting the data to a sigmoid model.

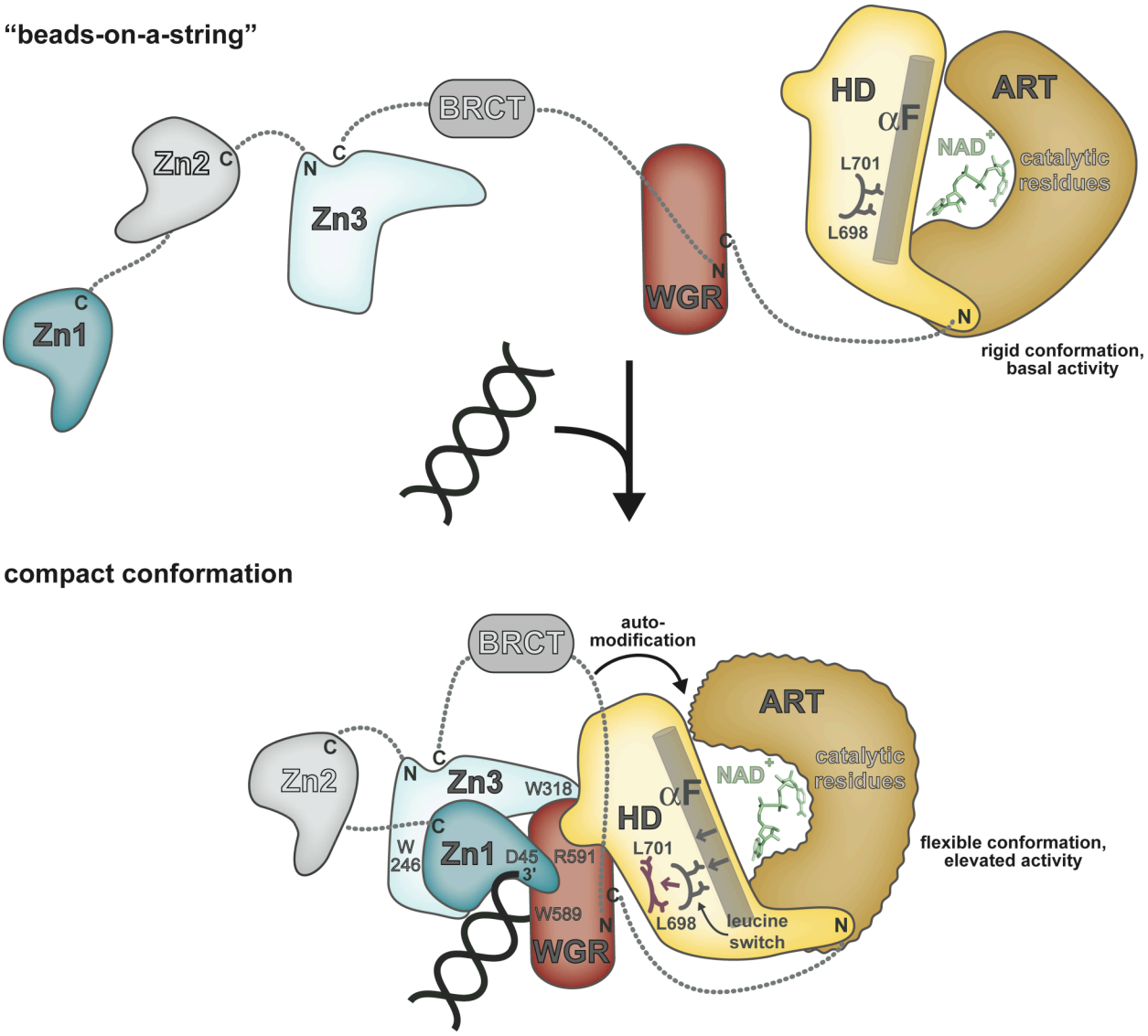

Fig. S11. Model for DNA-dependent activation of PARP-1. Schematic model of PARP-1 "beads-on-a-string" conformation in the absence of DNA, and the compact conformation that forms upon binding to DNA damage. PARP-1 domains are labeled and colored as in Fig. 1A. The connectivity of PARP-1 domains is illustrated by dotted lines linking the N- and C-termini. Distortions of the HD that modulate ART subdomain catalytic activity are represented by the 'leucine switch' that re-positions leucine residues 698 and 701 (L698 and L701, respectively) and the movement of αF. Critical residues at domain interfaces are labeled. NAD^+ marks the catalytic active site of the ART subdomain. We propose that in the absence of DNA, the native HD structure maintains the ART in a quiescent state with low flexibility and dynamics, thus holding PARP-1 catalytic activity at a low basal level (top). In the presence of DNA damage, the DNA-dependent regulatory domains flip the 'leucine switch' and consequently alter the flexibility and dynamics of the ART (bottom). Protein dynamics and conformational flexibility are critical for enzyme catalyzed reactions (*44-47*), and they are particularly important for multi-step enzymatic reactions, such as the poly(ADP-ribosyl)ation reaction catalyzed by PARP-1, which involves initial modification of a protein side chain, repeated cycles of NAD^+ binding and hydrolysis and re-positioning of a growing polymer chain. An increase in protein dynamics and flexibility of the ART upon DNA-dependent PARP-1 assembly is proposed to increase the efficiency of these steps leading to a higher catalytic turnover.

Table S1: Crystallographic data and refinement statistics

Data Collection[a]			
	PARP-1/DNA Complex		
Space Group Unit Cell Dimensions	$P2_12_12_1$ *a*=65.1 Å, *b*=113.0 Å, *c*=294.7 Å α=γ=β=90°		
Crystal	Crystal 65	Crystal 65 zinc edge	Crystal Se19 selenium edge
Wavelength (Å)	1.075	1.283	0.979
Resolution range (Å)	50–3.25 (3.31–3.25)	50–4.0 (4.21–4.00)	50–5.0 (5.26–5.00)
Completeness (%)	94.7 (98.2)	99.4 (97.9)	99.3 (96.7)
Average Redundancy	4.8 (4.5)	6.3 (6.3)	7.7 (7.8)
Mean I/σ(I)	12.1 (1.5)	15.0 (2.5)	7.2 (3.5)
R_{merge} (%)[b]	0.093 (0.672)	0.058 (0.807)	0.167 (0.461)
Model Refinement[a]			
Resolution Range (Å)	20–3.25 (3.38–3.25)		
Number of reflections	31,628 (2100)		
R_{cryst}[c]	0.238 (0.365)		
R_{free}[c]	0.304 (0.407)		
Number of atoms / Average B-factor (Å^2)	11,750/178.6		
protein	10,682/181.1		
DNA	1,060/154.6		
Phi/Psi, most favored (%)	93.9		
R.m.s.d. bond angles (°)	0.950		
R.m.s.d. bond lengths (Å)	0.006		

[a] Values in parentheses refer to data in the highest resolution shell.

[b] $R_{merge} = \sum_{hkl}\sum_j | I_j - \langle I \rangle | \ / \ \sum_{hkl}\sum_j I_j$. $\langle I \rangle$ is the mean intensity of *j* observations of reflection *hkl* and its symmetry equivalents.

[c] $R_{cryst} = \sum_{hkl} | F_{obs} - kF_{calc} | / \sum_{hkl} | F_{obs} |$. $R_{free} = R_{cryst}$ for 5% of reflections excluded from crystallographic refinement.

Table S2

Domain–domain interface statistics as reported by PDBsum (*48*).					
Interface	**# of residues**	**Interface area (Å^2)**	**# of salt bridges**	**# of hydrogen bonds**	**# of non-bonded contacts**
Zn1:Zn3	9:9	496:482	–	5	64
Zn1:WGR	6:8	290:232	1	4	40
Zn3:WGR	4:4	262:254	–	–	16
Zn3:CAT	4:5	227:217	–	1	23
WGR:CAT	17:17	1001:924	–	4	64

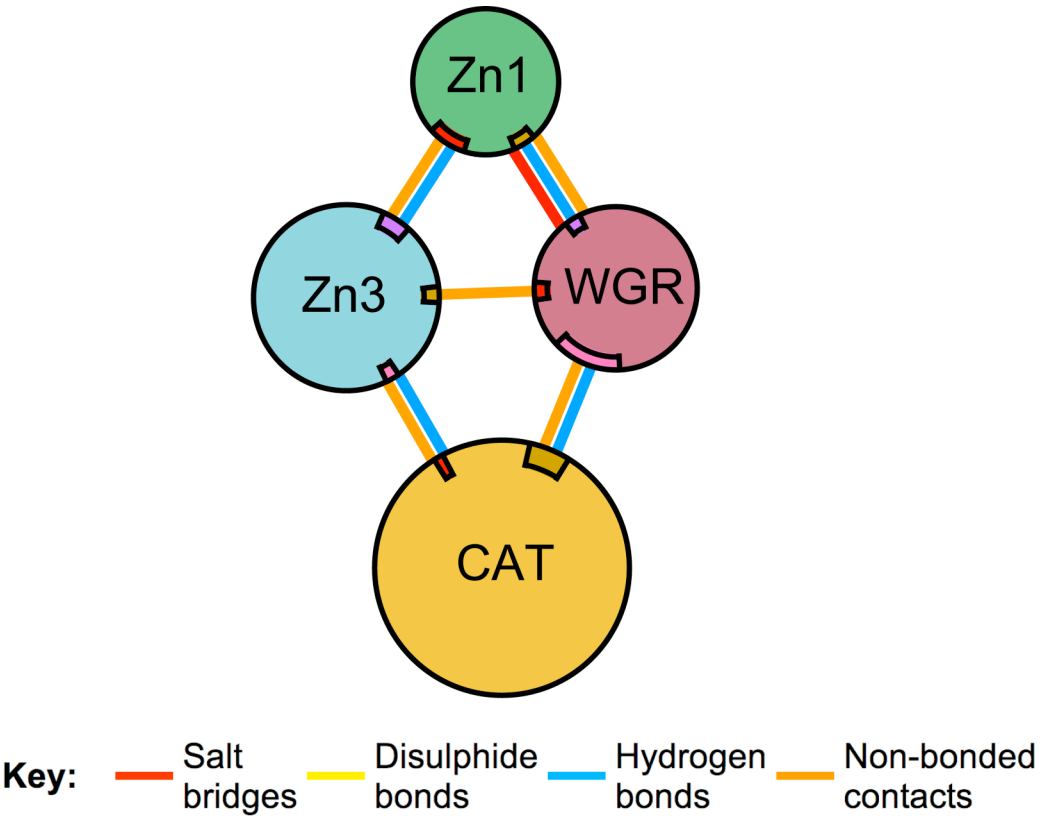

Domain–DNA interface areas (in Å) as calculate by AREAIMOL (*31*).				
	Zn1	**Zn3**	**WGR**	**CAT**
5′ DNA strand	130.1	35.8	245.5	0
3′ DNA strand	373.7	98.6	0	0

Supplementary References

25. M. F. Langelier, J. L. Planck, K. M. Servent, J. M. Pascal, *Methods Mol Biol* **780**, 209 (2011).
26. G. D. Van Duyne, R. F. Standaert, P. A. Karplus, S. L. Schreiber, J. Clardy, *J Mol Biol* **229**, 105 (Jan 5, 1993).
27. R. C. Benjamin, D. M. Gill, *J Biol Chem* **255**, 10493 (Nov 10, 1980).
28. Z. a. M. Otwinowski, W., in *Methods in Enzymology,* J. Carter, C.W. and Sweet, R.M., Ed. (Academic, New York, 1997), vol. 276, pp. 307 - 326.
29. W. Kabsch, *Acta Crystallogr D Biol Crystallogr* **66**, 125 (Feb, 2010).
30. A. J. McCoy, *Acta Crystallogr D Biol Crystallogr* **63**, 32 (Jan, 2007).
31. Collaborative Computational Project, *Acta Crystallogr D Biol Crystallogr* **50**, 760 (Sep 1, 1994).
32. M. Strong *et al.*, *Proc Natl Acad Sci U S A* **103**, 8060 (May 23, 2006).
33. P. Emsley, K. Cowtan, *Acta Crystallogr D Biol Crystallogr* **60**, 2126 (Dec, 2004).
34. P. Schuck, *Biophys J* **78**, 1606 (Mar, 2000).
35. P. Schuck, in *Modern Analytical Ultracentrifuge: Techniques and Methods,* D. J. Scott, Harding, S.E., Rowe, A.J., Ed. (The Royal Society of Chemistry, Cambridge, 2005) pp. 26-60.
36. H. Mendoza-Alvarez, R. Alvarez-Gonzalez, *J Biol Chem* **268**, 22575 (Oct 25, 1993).
37. E. Pion *et al.*, *Biochemistry* **44**, 14670 (Nov 8, 2005).
38. S. Messner *et al.*, *Nucleic Acids Res* **38**, 6350 (Oct, 2010).
39. Z. Tao, P. Gao, H. W. Liu, *J Am Chem Soc* **131**, 14258 (Oct 14, 2009).
40. M. Ikejima *et al.*, *J Biol Chem* **265**, 21907 (Dec 15, 1990).
41. O. Huambachano, F. Herrera, A. Rancourt, M. S. Satoh, *J Biol Chem* **286**, 7149 (Mar 4, 2011).
42. E. Le Cam *et al.*, *J Mol Biol* **235**, 1062 (Jan 21, 1994).
43. S. Hayward, H. J. Berendsen, *Proteins* **30**, 144 (Feb 1, 1998).
44. N. Doucet, E. D. Watt, J. P. Loria, *Biochemistry* **48**, 7160 (Aug 4, 2009).
45. E. D. Watt, H. Shimada, E. L. Kovrigin, J. P. Loria, *Proc Natl Acad Sci U S A* **104**, 11981 (Jul 17, 2007).
46. M. Wolf-Watz *et al.*, *Nat Struct Mol Biol* **11**, 945 (Oct, 2004).
47. P. Zavodszky, J. Kardos, Svingor, G. A. Petsko, *Proc Natl Acad Sci U S A* **95**, 7406 (Jun 23, 1998).
48. R. A. Laskowski *et al*., *Trends Biochem Sci* **22**, 488 (Dec, 1997).